Improvement of numerical simulation for GMAW based on a new model with thermocapillary effect

Jiang, Yongyue; Lin, Ping

Published in:
Journal of Computational and Applied Mathematics

DOI:
10.1016/j.cam.2019.01.039

Publication date:
2019

Improvement of numerical simulation for GMAW based on a new model with thermocapillary effect

Yongyue Jiang[1, 2, *], Ping Lin[3]

[1]iSinoNet Technology Co., Ltd., Fengxiu Middle Road No. 3, Beijing, 100094.
[2]School of Civil & Environmental Engineering, University of Science and Technology Beijing, Beijing, 100083.
3Department of Mathematics, University of Dundee, Dundee DD1 4HN, Scotland, United Kingdom.
[*]Corresponding author, E-mail: jiangyongyue1987@sina.com

In this paper, we present a numerical investigation about the metal transfer of GMAW with a new model based on the phase field model. Unlike most published work, the thermocapillary effect and mixture energy resulting from the newly research of multiphase fluids are taken into model of phase transfer and interface change which is different from volume of fluid method (VOF) that has been widely used in welding problem. We discretize the whole model including continuity condition, Navier-Stokes equation, phase field model, energy equation and Maxwell's equations with a continuous finite element method in space and a midpoint scheme in time and a penalty formulation is applied to the continuity condition due to the stability in the pressure. Metal transfer of GMAW with pulse current is computed as a numerical example where the numerical result have been verified by the experimental data obtained by using a high-speed camera. Moreover, we also compare the numerical results with and without considering the thermocapillary effects to show that the new model has a higher precision in predicting the droplet in welding.

Key words GMAW, thermocapillary effect, mixture energy, phase field model, finite element method.

Introduction

Gas metal arc welding (GMAW) is one kind of arc welding which uses the arc composed of an electron flow and electrically neutral arc plasma under the shielding gas to melt the moving wire and work-piece. With the advantage such as low cost, easy operation and good adaptability, GMAW process is an indispensable technology in various fields of industry, for example, steel structure, hydraulic electro-generating and food mechanism and so on. However, GTAW has a higher welding quality than GMAW and this is the reason that GTAW is always chosen for aerospace, even though with a higher cost. In GMAW, wire and workpiece serve as the two terminals of the arc, cathode and anode. The tip of the welding wire melts to be droplet due to surface tension at high temperature coming from arc, Ohmic heating and electrode heating and falls into the weld pool when the sum of the resultant forces include gravity, electromagnetic force, arc pressure and arc plasma force overcome the resistance of surface tension. This whole process is called metal transfer which involves not only effect of multi-field coupling including electromagnetic effect, fluid flow, heat and mass transfer but also phase transfer and interface structure change. It plays an important role in GMAW as the size and the frequency of falling droplet would have a

significant influence on the welding process quality and metal transfer has been investigated extensively both theoretically and experimentally for the better welding quality. Mckelliget and Szekely [1] investigated temperature distribution of electrode and weld pool with a two-dimensional theoretical model earlier but steady and without consideration of dynamics of droplet. This steady model also used to study the properties of free-burning arc columns and the cathode by Lowke et al. [2]. Then Haidar and Lowke [3] presented an investigation about the influence of different value of current on the size of droplets with an unsteady model which might be closer to reality. Wu, Zhong and Gao [4] developed an experimental system to investigate the dynamics of weld pool and hump formulation during high-speed GMAW. The experiment about the surface temperature of the deposited thin-wall parts was carried out by Yang, Wang and Zhang [5]. They used an infrared camera after calibration to capture the temperature and investigated the thermal behavior in GMAW of additive manufacturing. Tipi, Sani and Pariz [6] designed an experiment based on a three-layer cascade control strategy to control the detachment frequency in GMAW. This method made the drop detaching more regularity. A unified numerical model is developed to clarify the droplet transfer phenomena during a VP-GMAW process by Zhao and Chung [7] with the consideration of the interaction between the arc plasma and the moving droplet. Cheng, Wu and Lian [8] presented a dynamic model for metal transfer combined electromagnetic theory with volume of fluid (VOF) considering electromagnetic force, surface tension and arc plasma. There are also some numerical researches about fume formation and vapor in GMAW [9-12].

The motivation of the previous work about the numerical simulation of metal transfer in GMAW including the work mentioned above is to study dynamics and geometry of the droplet with the effect of multiple parameters like arc plasma, vapor, fume and varieties of force. The theoretical model based on some conservation law like momentum and energy for simulating the metal transfer in GMAW widely used before contains Navier-Stokes equations, VOF (model of free surface) which couples volume fraction of fluid with velocity, energy equation refer to temperature and Maxwell equations. They use this theoretical model to analyze the velocity, current density, temperature and free surface with additional terms resulting from varieties of forces or considering different energy, even the new model of concentration. Actually, the previous work ignores the influence of multiple parameters on the geometry of the droplet and free surface, especially the direct influence of temperature. According to the newly research about the dynamics of interface in multi-phase fluids or may be earlier, thermocapillary effect popular in Marangoni convection [20] plays an important role in the multi-phase fluids system where the surface tension becomes dominant [13-15]. The drop set in a liquid possessing a temperature gradient will move towards the hot region due to the thermocapillary effect which is called thermocapillary migration of drops. Surface tension that keeps droplet as a ball and stops the droplet detaching from the molten wire playing an important role in in metal transfer before the breakup [16]. This effects indicates that the theoretical model should consider the thermocapillary effect especially for the process of GMAW having temperature change with a large scale.

In addition, the system of metal transfer in GMAW is a mixture which is not considered in the previous work composed of wire, molten metal and droplet. This mixture energy has an effect on the phase transfer and interface change which has already been introduced to the phase field model for multi-phase fluid with clear interface [17-19]. Different phases in phase field model are treated as one phase and are mixed smoothly in the vicinity of the interface where the flow parameters should change rapidly referred to sharp interface model [20, 22]. Compared with VOF, phase field model may be more suitable for the numerical simulation of metal transfer as this method introduces the thickness of interface into the model which do not exists in VOF. The physical property parameters like density, capacity and conductivity change continuously from one phase to the other phase during the thickness of the interface and this can make the molten zone more clearly and also can be easier to simulate the dynamics of interface. In phase field model, it does not regard the interface as boundary and it avoids dealing with the jump of boundary conditions.

However, there is no thickness between different phases in the mixture or the thickness of the interface is nanometer scale in the real world. So the validity of the phase field model should be examined when the thickness tends to zero or nanometer scale which is also called sharp interface limit. But it is difficult to compute the result of phase field model when the thickness is nanometer scale, and then a criterion of sharp interface limit [17] for moving contact line is proposed which makes the examination easier. In this paper, a new theoretical model for metal transfer in GMAW focusing on the phase transfer and interface change based on the phase field model is proposed with the consideration of thermocapillary effect and mixture energy. In [25], Zhao and Chung used phase field model to simulate the metal transfer from globular to spray transfer with the consideration of mixed energy, but they did not consider the thermocapillary effect and the couple effect of thermocapillary and mixed energy. Also, they did not couple the phase field model with the energy equation as they applied the hypothesis of melting velocity equalling to the wire feed rate.

In Section 1, the model, boundary conditions and continuous weak formulation are introduced. The fully discretized GMAW system with a continuous finite element method and a second order temporal scheme is presented in Section 2. A numerical example with pulse current is computed and the numerical result and discussion are shown in Section 3. Section 4 is the conclusion.

The new model for GMAW and weak form

Fig. 1 shows the general physical model of GMAW. Due to the symmetry of the GMAW system, the metal transfer behavior can be simplified to a 2D axial symmetry system. The welding region is defined as Ω a bounded domain and Γ is the boundary of Ω. C is the shielding gas nozzle ejecting the inert shielding gas to prevent the molten metal from oxidation. $AB+BC+CD+DE+EF+FG+GA$ is the half domain of Ω.

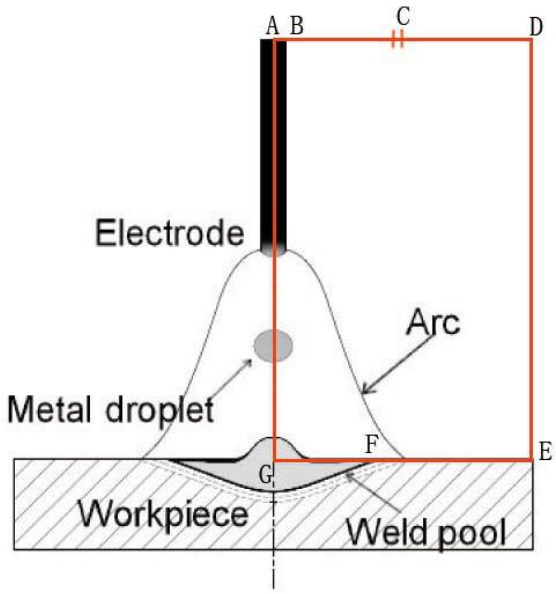

Fig. 1 The simple structure of GMAW system

The new model with phase field model for GMAW is shown as follows (Eq. (3) and (4) are the phase field model of Cahn-Hilliard type):

$$\frac{\partial \rho}{\partial t}+\nabla\cdot(\rho\mathbf{v})=0 \tag{1}$$

$$\frac{\partial(\rho\mathbf{v})}{\partial t}+\nabla\cdot(\rho\mathbf{v}\otimes\mathbf{v})=-\nabla p+\nabla\cdot\left(\eta\left(\nabla\mathbf{v}+\nabla\mathbf{v}^{\mathrm{T}}\right)\right)-\nabla\cdot\left(\lambda_f\left(\nabla f\otimes\nabla f\right)\right)+\mu\nabla f-\rho\mathbf{G}+\mathbf{J}\times\mathbf{B}+\rho\mathbf{G}\beta_T\left(T-T_0\right) \tag{2}$$

$$\frac{\partial(\rho f)}{\partial t}+\nabla\cdot(\rho \mathbf{v} f)=\nabla\cdot(M\nabla\mu) \tag{3}$$

$$\mu=\lambda_f\frac{f\left(f^2-1\right)}{\varepsilon}-\lambda_f\varepsilon\Delta f \tag{4}$$

$$\frac{\partial(\rho c_p T)}{\partial t}+\nabla\cdot(\rho c_p \mathbf{v} T)=\nabla\cdot(k\nabla T+M\mu\nabla\mu)-\rho H\frac{\partial f}{\partial t}+\frac{\mathbf{J}^2}{\sigma_e}+\frac{5k_b}{2e}\mathbf{J}\cdot\nabla T \tag{5}$$

$$\nabla\cdot(\sigma_e\nabla\Phi)=0\mathbf{J}=-\sigma_e\nabla\Phi,\Delta\mathbf{A}=-\mu_0\mathbf{J},\mathbf{B}=\nabla\times\mathbf{A} \tag{6}$$

Here β_T, M, ε are the thermal expansion coefficient, phenological mobility coefficient, thickness of interface, respectively. ρ, η, k, c_p represent the density, viscosity, thermal conductivity coefficient, specific heat, respectively. k_b, e, σ_e denote Stefan-Boltzmann constant, electronic charge and electrical conductivity, respectively. μ is called chemical potential that represents the mixture energy as it has two parts contributing to separation and mixing, respectively. **v**, **J** are the velocity and current density. f is the order parameter for defining different phases of the mixture ($f=1$: fluid and $f=-1$: metal) and T represents temperature. The third and fourth terms on the right-hand side of Eq. (2) represent the modified surface tension and capillary force due to the mixture energy and thickness of interface introduced in the model. The last three terms on the right-hand side of Eq. (2) denote gravity, electro-magnetic force and bouyancy force due to high temperature, respectively. Φ, **B** are the electrical potential and self-induced electro-magnetic field. **A**, T_0 are magnetic vector and initial temperature. λ_f is a coefficient but a function of temperature $\lambda_f=\eta\varepsilon\sigma_0-\eta\varepsilon\sigma_T\left(T-T_0\right)$ refers to thermocapillary effect. The first term on the right side of Eq. (5) represents the modified Fourier diffusion flux and the second term is used to define the latent heat of fusion. And the last two terms of Eq. (5) are Ohmic heating and energy transfer due to electron flow, respectively. The boundary conditions and computing domain in the previous work of Hu and Tsai [16] are used in this paper. The additional boundary conditions for f and μ are $\partial_{\mathbf{n}} f=0, \partial_{\mathbf{n}}\mu=0$ which is listed in Table 1. v_w is the wire feed rate, the radial component of the inflow of gas from the nozzle is onitted and $v(r)$ represents the axial velocity component defined by Eq. (7) [24] ,

$$v(r)=\frac{2Q}{\pi}\frac{\left(R_n^2-r^2+\left(R_n^2-R_c^2\right)\dfrac{\ln(r/R_n)}{\ln(R_n/R_c)}\right)}{R_n^4-R_c^4+\dfrac{\left(R_n^2-R_c^2\right)^2}{\ln(R_n/R_c)}}+v_w\frac{\ln(R_n/r)}{\ln(R_n/R_c)} \tag{7}$$

where Q is the inflow rate of the shielding gas, R_c is the radius of the electrode, R_n is the internal radius of the shielding gas nozzle.

Table 1 The boundary conditions for the computing domain

	AB	BC	CD	DE	EF	FG	GA
v	$\mathbf{v}\cdot\mathbf{n}=v_w$	$\mathbf{v}\cdot\mathbf{n}=v(r)$	$\partial_{\mathbf{n}}\mathbf{v}=0$	$\partial_{\mathbf{n}}\mathbf{v}=0$	0	0	$\partial_{\mathbf{n}}\mathbf{v}=0$
T	300K	300K	300K	300K	300K	300K	$\partial_{\mathbf{n}}T=0$
Φ	$\sigma_e\partial_{\mathbf{n}}\Phi=I(\pi R_c^2)^{-1}$	$\partial_{\mathbf{n}}\Phi=0$	$\partial_{\mathbf{n}}\Phi=0$	$\partial_{\mathbf{n}}\Phi=0$	0	0	$\partial_{\mathbf{n}}\Phi=0$
f	$\partial_{\mathbf{n}}f=0$	$\partial_{\mathbf{n}}f=0$	$\partial_{\mathbf{n}}f=0$	$\partial_{\mathbf{n}}f=0$	$\partial_{\mathbf{n}}f=0$	$\partial_{\mathbf{n}}f=0$	$\partial_{\mathbf{n}}f=0$

μ	$\partial_{\mathbf{n}}\mu=0$	$\partial_{\mathbf{n}}\mu=0$	$\partial_{\mathbf{n}}\mu=0$	$\partial_{\mathbf{n}}\mu=0$	$\partial_{\mathbf{n}}\mu=0$	$\partial_{\mathbf{n}}\mu=0$	$\partial_{\mathbf{n}}\mu=0$

As the densities of molten metal and solid metal are matched and work of Abels et al. [21], the model of the system can be simplified in the next form ($\mathbf{H}=\rho M\nabla\mu/2$ represents the mass flux due to the continuity condition based on different densities)

$$\nabla\cdot\mathbf{v}=0 \tag{8}$$

$$\rho\frac{\partial\mathbf{v}}{\partial t}+\rho(\mathbf{v}\cdot\nabla)\mathbf{v}=-\nabla p+\eta\Delta\mathbf{v}-\nabla\cdot\left(\lambda_f(\nabla f\otimes\nabla f)\right)+\mu\nabla f-\rho\mathbf{G}+\mathbf{J}\times\mathbf{B}+\rho\mathbf{G}\beta_T(T-T_0)-\mathbf{H}\cdot\nabla\mathbf{v} \tag{9}$$

$$\frac{\partial f}{\partial t}+\mathbf{v}\cdot\nabla f=M\Delta\mu,\quad \mu=\lambda_f\frac{f(f^2-1)}{\varepsilon}-\lambda_f\varepsilon\Delta f \tag{10}$$

$$\rho c_p\frac{\partial T}{\partial t}+\rho c_p\mathbf{v}\cdot\nabla T=\nabla\cdot(k\nabla T+M\mu\nabla\mu)-\rho H\frac{\partial f}{\partial t}+\frac{\mathbf{J}^2}{\sigma_e}+\frac{5k_b}{2e}\mathbf{J}\cdot\nabla T \tag{11}$$

$$\nabla\cdot(\sigma_e\nabla\Phi)=0,\ \mathbf{J}=-\sigma_e\nabla\Phi,\ \Delta\mathbf{A}=-\mu_0\mathbf{J},\ \mathbf{B}=\nabla\times\mathbf{A} \tag{12}$$

In order to enhance the stability of computing [18, 20], a positive constant c is introduced to rewrite Eq. (10) as

$$\frac{\partial f}{\partial t}+\mathbf{v}\cdot\nabla f=M\Delta(\omega+cf),\ \omega+cf=\mu. \tag{13}$$

The penalty formulation [18] is applied to Eq. (8) for the stability in the computation of pressure to reformulate the continuity condition from index-2 problem to an index-1 problem with $\nabla\cdot\mathbf{v}+\delta p=0$ where δ is small penalty.

Denote $\mathbf{W}^{1,3}(\Omega)=\left(W^{1,3}(\Omega)\right)^3\mathbf{L}^2(\Omega)=\left(L^2(\Omega)\right)^2$ and $L_0^2(\Omega)=\left\{p\in L^2(\Omega),\int_\Omega p\,d\mathbf{x}=0\right\}$. The weak form of the penalized GMAW system reads: Find $\mathbf{v},\mathbf{J},\mathbf{B},\mathbf{A}\in\mathbf{W}^{1,3}(\Omega)$, $p\in L_0^2(\Omega)$, f, μ, Φ, $T\in W^{1,3}(\Omega)$ such that

$$\int_\Omega(\nabla\cdot\mathbf{v}+\delta p)q d\mathbf{X}=0 \qquad \forall q\in L_0^2(\Omega) \tag{14}$$

$$\int_\Omega\Big(\rho\frac{\partial\mathbf{v}}{\partial t}\cdot\mathbf{u}+\rho(\mathbf{v}\cdot\nabla)\mathbf{v}\cdot\mathbf{u}-p(\nabla\cdot\mathbf{u})+\eta\nabla\mathbf{v}:\nabla\mathbf{u}+\rho\mathbf{G}\cdot\mathbf{u}-(\mathbf{J}\times\mathbf{B})\cdot\mathbf{u}-\rho\mathbf{G}\beta_T(T-T_0)\cdot\mathbf{u}-(\omega+cf)\nabla f\cdot\mathbf{u}$$
$$+\lambda_f(\nabla f\otimes\nabla f):\nabla\mathbf{u}+\mathbf{H}\cdot\nabla\mathbf{v}\cdot\mathbf{u}\Big)d\mathbf{X}+\int_\Gamma p(\mathbf{n}\cdot\mathbf{u})ds=0 \qquad \forall\mathbf{u}\in\mathbf{W}^{1,3} \tag{15}$$

$$\int_\Omega\left(\frac{\partial f}{\partial t}\gamma+(\mathbf{v}\cdot\nabla f)\gamma+M\nabla(\omega+cf)\cdot\nabla\gamma\right)d\mathbf{X}=0 \qquad \forall\gamma\in W^{1,3} \tag{16}$$

$$\int_\Omega\left((\omega+cf)\chi-\lambda_f\frac{f(f+1)(f-1)}{\varepsilon}\chi-\lambda_f\varepsilon\nabla f\cdot\nabla\chi\right)d\mathbf{X}=0 \qquad \forall\chi\in W^{1,3} \tag{17}$$

$$\int_\Omega\left(\rho c_p\left(\frac{\partial T}{\partial t}+\mathbf{v}\cdot\nabla T\right)\theta+k\nabla T\cdot\nabla\theta+\rho H\frac{\partial f}{\partial t}\theta-\frac{\mathbf{J}^2}{\sigma_e}\theta+M(\omega+cf)\nabla(\omega+cf)\cdot\nabla\theta-\frac{5k_b}{2e}\mathbf{J}\cdot\nabla T\theta\right)d\mathbf{X}=0$$
$$\forall\theta\in W^{1,3} \tag{18}$$

$$\int_\Omega(\nabla\mathbf{A}:\nabla\boldsymbol{\alpha}+\mu_0\sigma_e\nabla\Phi\cdot\boldsymbol{\alpha})d\mathbf{X}-\int_\Gamma(\mathbf{n}\cdot\nabla\mathbf{A})\cdot\boldsymbol{\alpha}ds=0,\qquad\int_\Omega(\sigma_e\nabla\Phi\cdot\nabla\varphi)d\mathbf{X}-\int_\Gamma\sigma_e(\mathbf{n}\cdot\nabla\Phi)\varphi ds=0,$$

$$\int_\Omega \left(\mathbf{J}+\sigma_e \nabla\Phi\right)\cdot\mathbf{S}\, d\mathbf{X}=0,\ \int_\Omega \left(\mathbf{B}-\nabla\times\mathbf{A}\right)\cdot\mathbf{L}\, d\mathbf{X}=0 \qquad \forall \boldsymbol{\alpha},\varphi,\mathbf{S},\mathbf{L}\in\mathbf{W}^{1,3} \quad (19)$$

Finite element scheme and fully discretized GMAW system

The solution of the weak form is approximated by a finite difference scheme in time and a conformal C^0 finite element method in space. $\Delta t>0$ denotes the time step size and $\mathbf{v}_h^n, p_h^n, f_h^n, \omega_h^n, \mathbf{J}_h^n, \mathbf{B}_h^n, \mathbf{A}_h^n, T_h^n, \Phi_h^n$ is an approximation of $\mathbf{v}\left(t^n\right)=\mathbf{v}\left(n\Delta t\right), p\left(t^n\right)=p\left(n\Delta t\right), \Phi\left(t^n\right)=\Phi\left(n\Delta t\right)$, $f\left(t^n\right)=f\left(n\Delta t\right), \omega\left(t^n\right)=\omega\left(n\Delta t\right), \mathbf{J}\left(t^n\right)=\mathbf{J}\left(n\Delta t\right), \mathbf{B}\left(t^n\right)=\mathbf{B}\left(n\Delta t\right), \mathbf{A}\left(t^n\right)=\mathbf{A}\left(n\Delta t\right), T\left(t^n\right)=T\left(n\Delta t\right)$ And $\mathbf{v}_h^{n+1}, p_h^{n+1}, f_h^{n+1}, \omega_h^{n+1}, \mathbf{J}_h^{n+1}, \mathbf{B}_h^{n+1}, \mathbf{A}_h^{n+1}, T_h^{n+1}, \Phi_h^{n+1}$ is the approximation at time $t^{n+1}=\left(n+1\right)\Delta t$. The weak form is treated with the modified midpoint scheme [18] and the discretized formulation reads:

$$\int_\Omega \left(\nabla\cdot\mathbf{v}_h^{n+1/2}+\delta p_h^{n+1/2}\right)q d\mathbf{X}=0 \quad (20)$$

$$\int_\Omega \left(\rho\mathbf{v}_{\bar{t}}^{n+1}\cdot\mathbf{u}+\rho\left(\mathbf{v}_h^{n+1/2}\cdot\nabla\right)\mathbf{v}_h^{n+1/2}\cdot\mathbf{u}-p_h^{n+1/2}\left(\nabla\cdot\mathbf{u}\right)+\eta\nabla\mathbf{v}_h^{n+1/2}:\nabla\mathbf{u}+\rho\mathbf{G}\cdot\mathbf{u}-\left(\mathbf{J}_h^{n+1/2}\times\mathbf{B}_h^{n+1/2}\right)\cdot\mathbf{u}-\rho\mathbf{G}\beta_T\left(T_h^{n+1/2}-T_0\right)\cdot\mathbf{u}\right.$$
$$\left.-\left(\omega_h^{n+1/2}+cf_h^{n+1/2}\right)\nabla f_h^{n+1/2}\cdot\mathbf{u}+\lambda_f\left(\nabla f_h^{n+1/2}\otimes\nabla f_h^{n+1/2}\right):\nabla\mathbf{u}+\mathbf{H}^{n+1/2}\cdot\nabla\mathbf{v}^{n+1/2}\cdot\mathbf{u}\right)d\mathbf{X}+\int_\Gamma p_h^{n+1/2}\left(\mathbf{n}\cdot\mathbf{u}\right)ds=0 \quad (21)$$

$$\int_\Omega \left(f_{\bar{t}}^{n+1}\gamma+\left(\mathbf{v}_h^{n+1/2}\cdot\nabla f_h^{n+1/2}\right)\gamma+M\nabla\left(\omega_h^{n+1/2}+cf_h^{n+1/2}\right)\cdot\nabla\gamma\right)d\mathbf{X}=0 \quad (22)$$

$$\int_\Omega \left(\left(\omega_h^{n+1/2}+cf_h^{n+1/2}\right)\chi-P\left(f_h^n,f_h^{n+1}\right)\chi-\lambda_f\nabla f_h^{n+1/2}\cdot\nabla\chi\right)d\mathbf{X}=0 \quad (23)$$

$$\int_\Omega \left(\rho c_p\left(T_{\bar{t}}^{n+1}+\mathbf{v}_h^{n+1/2}\cdot\nabla T_h^{n+1/2}\right)\theta+k\nabla T_h^{n+1/2}\cdot\nabla\theta+M\left(\omega_h^{n+1/2}+cf_h^{n+1/2}\right)\nabla\left(\omega_h^{n+1/2}+cf_h^{n+1/2}\right)\cdot\nabla\theta+\rho H\frac{\partial f}{\partial t}\theta\right.$$
$$\left.-\frac{\left|\mathbf{J}_h^{n+1/2}\right|^2}{\sigma_e}\theta-\frac{5k_b}{2e}\mathbf{J}_h^{n+1/2}\cdot\nabla T_h^{n+1/2}\theta\right)d\mathbf{X}=0 \quad (24)$$

$$\int_\Omega \left(\nabla\mathbf{A}_h^{n+1/2}:\nabla\boldsymbol{\alpha}+\mu_0\sigma_e\nabla\Phi_h^{n+1/2}\cdot\boldsymbol{\alpha}\right)d\mathbf{X}-\int_\Gamma\left(\mathbf{n}\cdot\nabla\mathbf{A}_h^{n+1/2}\right)\cdot\boldsymbol{\alpha}ds=0,\int_\Omega\left(\sigma_e\nabla\Phi_h^{n+1/2}\cdot\nabla\varphi\right)d\mathbf{X}-\int_\Gamma\sigma_e\left(\mathbf{n}\cdot\nabla\Phi_h^{n+1/2}\right)\varphi ds=0, \quad (25)$$

$$\int_\Omega\left(\mathbf{J}_h^{n+1/2}+\sigma_e\nabla\Phi_h^{n+1/2}\right)\cdot\mathbf{S}=0,\int_\Omega\left(\mathbf{B}_h^{n+1/2}-\nabla\times\mathbf{A}_h^{n+1/2}\right)\cdot\mathbf{L}=0. \quad (26)$$

Here $\mathbf{v}_h^{n+1/2}=\left(\mathbf{v}_h^{n+1}+\mathbf{v}_h^n\right)/2$, $p_h^{n+1/2}=\left(p_h^{n+1}+p_h^n\right)/2$, $\mathbf{v}_{\bar{t}}^{n+1}=\left(\mathbf{v}_h^{n+1}-\mathbf{v}_h^n\right)/\Delta t$, $\mathbf{J}_h^{n+1/2}=\left(\mathbf{J}_h^{n+1}+\mathbf{J}_h^n\right)/2$,

$\mathbf{B}_h^{n+1/2}=\left(\mathbf{B}_h^{n+1}+\mathbf{B}_h^n\right)/2$, $T_h^{n+1/2}=\left(T_h^{n+1}+T_h^n\right)/2$, $f_h^{n+1/2}=\left(f_h^{n+1}+f_h^n\right)/2$, $\Phi_h^{n+1/2}=\left(\Phi_h^{n+1}+\Phi_h^n\right)/2$,

$\mathbf{A}_h^{n+1/2}=\left(\mathbf{A}_h^{n+1}+\mathbf{A}_h^n\right)/2$, $P\left(f_h^n,f_h^{n+1}\right)=\lambda_f\left(f_h^{n+1}+f_h^n\right)\left(f_h^{n+1}+f_h^n-1\right)\left(f_h^{n+1}+f_h^n-2\right)/8\varepsilon^2$.

Numerical examples, result and discussion

In this section, the discrete system Eq. (20)-(26) is used to compute a numerical example. Stainless steel with 1.2 mm diameter is chosen as the electrode and the shielding gas is pure argon. The computations are carried out and the results are shown with the help of the FreeFem++ platform [23] and Tecplot. They are calculated under the P2 (piecewise polynomial of degree two) finite element space for

$\mathbf{v}, f, \omega, T, \mathbf{J}, \mathbf{A}, \mathbf{B}, \Phi$ and P1 finite element space for the pressure p. Table 1 shows the value of parameters used in the numerical simulation. Table 2 gives the value of parameters used in pulse current set as the welding current. Fig. 2 gives the wave of pulse current and four points (0, 1.377, 4.116, 7.231ms in one period) are chosen to show the numerical result of the discrete system. Only the interface structure is presented in Fig. 3. From Fig. 3a to Fig. 3b, as the current in peak time increases quickly, the amount of molten metal in wire increases and the droplet grows up. The necking effect also appears at the tip of the wire according to the numerical result. Compared with Fig. 3b and 3c, with the contribution to the electro-magnetic force in radial direction made by change of current and also the increase of the amount of molten metal refers to the gravity, the necking effect becomes more clearly. When the strain could not be held any more by the resistance like surface tension, in other words, the droplet breaks up in base time when the sum of gravity, electro-magnetic force and arc pressure overcome the resistance of surface tension (Fig. 3d) and becomes flat ellipse due to arc pressure gradient. The numerical result fits the theory of metal transfer well.

Table 2 Thermophysical properties of stainless steel and other parameter

Nomenclature	Symbol	Value (unit)
Specific heat of solid phase	c_s	$700\ \mathrm{J\cdot kg^{-1}\cdot K^{-1}}$
Specific heat of liquid phase	c_l	$780\ \mathrm{J\cdot kg^{-1}\cdot K^{-1}}$
Thermal conductivity of solid phase	k_s	$22\ \mathrm{W\cdot m^{-1}\cdot K^{-1}}$
Thermal conductivity of liquid phase	k_l	$22\ \mathrm{W\cdot m^{-1}\cdot K^{-1}}$
Density of solid phase	ρ_s	$7200\ \mathrm{kg\cdot m^{-3}}$
Density of liquid phase	ρ_l	$7200\ \mathrm{kg\cdot m^{-3}}$
Dynamic viscosity	η	$0.006\ \mathrm{kg\cdot m^{-1}\cdot s^{-1}}$
Latent heat of fusion	H	$2.47\times10^{5}\mathrm{J\cdot kg^{-1}}$
Electrical conductivity	σ_e	$7.7\times10^{5}\Omega^{-1}\cdot\mathrm{m^{-1}}$
Permeability	μ_0	$4\pi\times10^{-7}\mathrm{H\cdot m^{-1}}$
Thickness of the interface	ε	0.01 mm

Table 3 The time and current in one period of pulse for stainless steel

	Time（ms）	Current（A）
Peak	2.4	327
Project	3.0	106
Base	9.5	24

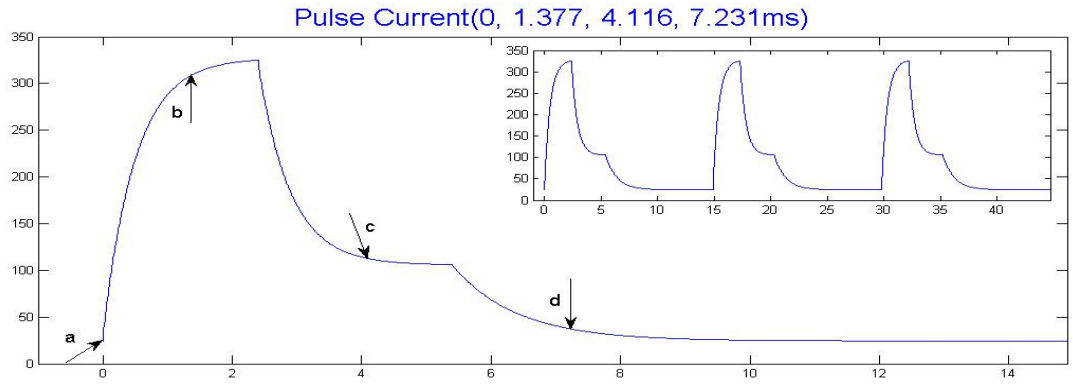

Fig. 2 The wave of pulse current (Large: One period; Small: Three periods)

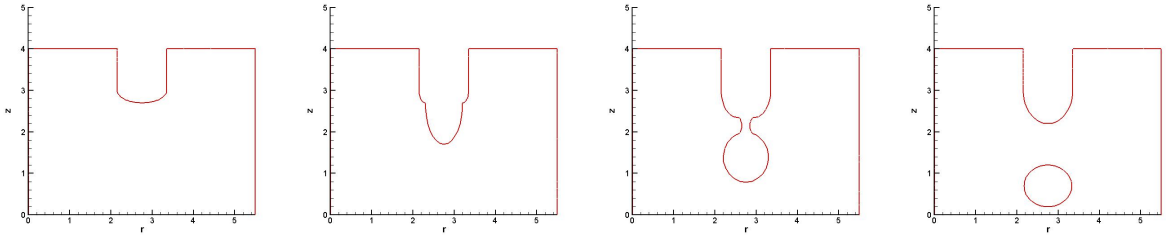

a **b** **c** **d**

Fig. 3 Evolution of interface structure of droplet and wire at t = 0, 1.377, 4.116, 7.231ms

The numerical result of droplet size is compared with the data of high-speed photography (Fig. 4) with the same conditions to identify the validity of this new model with the mark of (T, M/Y). The horizontal and vertical diameters at the time just before the droplet touches the weld pool are chosen, respectively. As the welding current is pulse current and one droplet for one period, every droplet for each period would have different size and geometry at the time just before the detached droplet touching the weld pool. So we verify the numerical solution with the data of high-speed photography which is the average value of 3000 periods (Fig. 5). The comparison in Table 2 including the numerical result of VOF model with the mark of (T, M/N) without thermocapillary effect and mixture energy under the same conditions shows that the result of new model agrees well with the data of high-speed photography. Also, the new model improves the precision in predicting the droplet size compared with VOF.

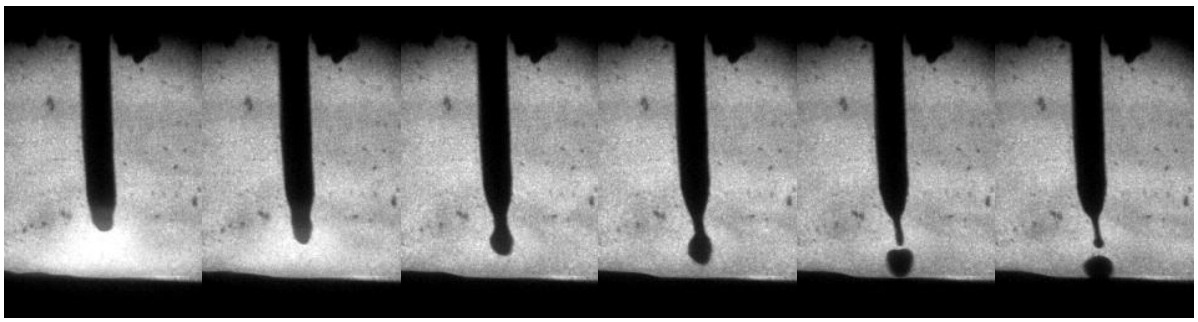

Fig. 4 Metal transfer captured by high-speed photography

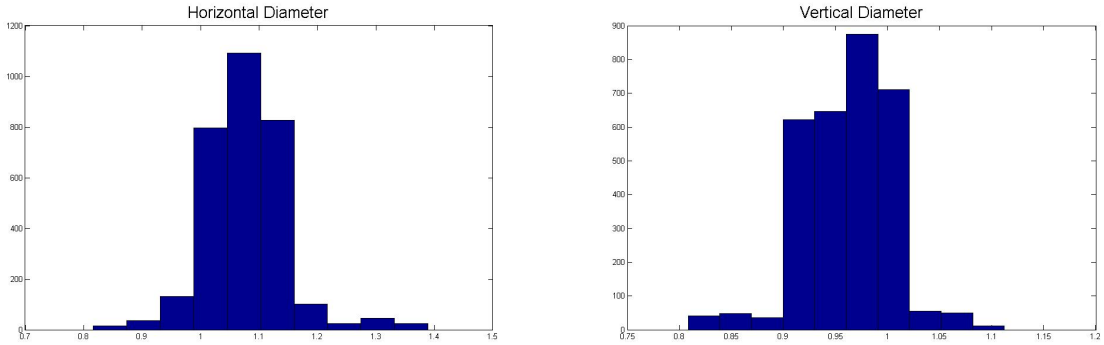

Fig. 5 The whole data of horizontal and vertical diameter in high-speed photography

Table 4 Comparison among high-speed photography, new model and VOF

	Horizontal Diameter	Vertical Diameter
High-speed photography	1.088mm	0.962mm
Numerical Simulations(T, M/Y)	1.169mm	1.053mm
Relative Error(T, M/Y)	7.444%	9.459%
Numerical Simulations(T, M/N)	1.287mm	1.116mm
Relative Error(T, M/N)	18.290%	16.008%

We also compare the numerical simulation with the experimental data of carbon steel of 1.2mm. We choose five points in the high-speed photography that we can verify the size and geometry of the droplet in the metal transfer of one period clearly. In Fig. 6, we give the pulse current of GMAW for carbon steel with diameter 1.2mm and average current 180A and the breakup time of numerical solution and experiment. We choose the velocity, accelerated speed, size to show the numerical solution and experimental data (average value of 3011 periods, Fig. 7 and Table 6, g is the gravity acceleration). The result shows that the numerical solution of new model and the data of high-speed photography fit quite well.

Table 5 The time and current in one period of pulse for carbon steel

	Time（ms）	Current（A）
Peak	0.63	531.7
Hold	0.81	531.7
Plunge	0.45	302.2
Project	1.72	102.0
Base	1.92	49.4

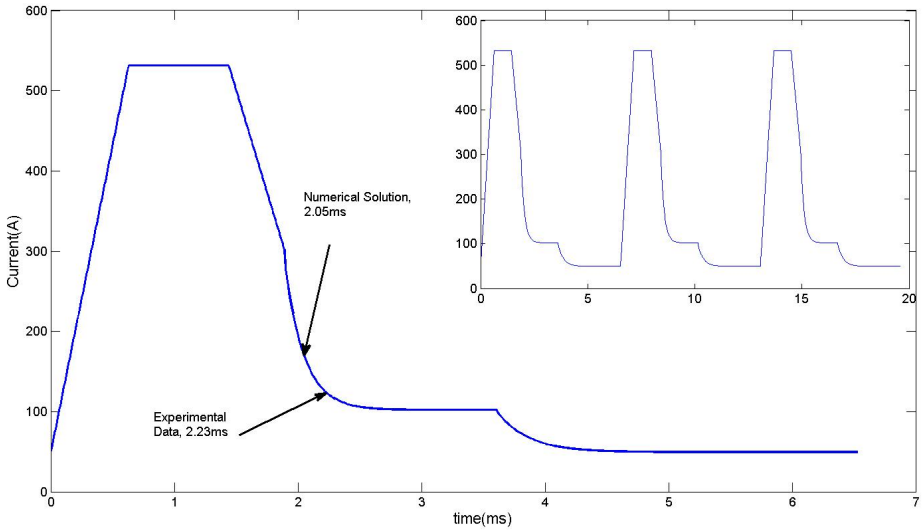

Fig. 6 Pulse current of 1.2mm carbon steel with average value 180A

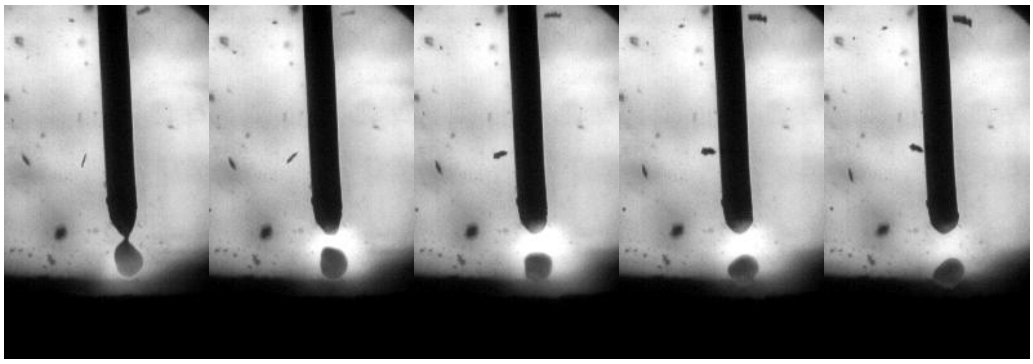

Fig. 7 Five points with clearly outline of metal transfer captured by high-speed photography

Table 6 Comparison among high-speed photography and new model for size, velocity and acceleration

	Horizontal(mm)	Vertical(mm)	Velocity($m \cdot s^{-1}$)	Acceleration/g
High-Speed photography	1.039 1.143 1.211 1.600 1.397	1.565 1.357 1.447 1.348 1.223	0.386 0.648 0.880 1.064 1.216	131.2 115.8 92.3 75.7
Numerical solution of the new model	1.133 1.305 1.491 1.607 1.641	1.532 1.416 1.302 1.137 1.053	0.411 0.712 0.959 1.170 1.346	150.1 123.7 105.9 87.3
Relative error	9.047% 4.173% 23.121% 0.437% 17.466%	2.109% 4.384% 10.021% 15.653% 13.900%	6.471% 9.877% 8.968% 9.962% 10.691%	14.405% 6.822% 14.735% 15.324%
Average value of relative error	10.848%	9.206%	9.197%	12.821%

Conclusion

In this paper, we present a numerical investigation of metal transfer in GMAW with a new model based on the phase field model and consider thermocapillary effect and mixture energy making the model more reasonable and the numerical simulation more practical. The continuous finite element method and a modified midpoint scheme are applied to solve the system and penalty formulation is used to enhance the stability of pressure. The metal transfer in GMAW with pulse current is examined to show that its numerical result fits the theory of dynamics of droplet in metal transfer quite well. Comparing with the data of high-speed photography, the validity of this new model has been validated due to the relatively smaller error of droplet diameter which is below 10%. We also show that the new model can make a higher precision in predicting the droplet size than the previous work making the numerical simulation closer to the reality. This new model and method could provide guiding function in predicting the geometry of droplet during the metal transfer which plays an important role in control of GMAW.

Acknowledgements

Yongyue Jiang is partially supported by Beijing Postdoctoral Research Foundation.

References

[1] Mckelliget J. and Szekely J. Heat transfer and fluid flow in the welding arc. Metallurgical Transactions A, 17 (7), 1139--1148 (1986).

[2] Lowke J. J., Kovitya P. and Schmidt H. P. Theory of free-burning arc columns including the influence of the cathode. Journal of Physics D: Applied Physics, 25 (25), 1600--1606 (1992).

[3] Haidar J., and Lowke J. J. Predictions of metal droplet formation in arc welding. Journal of Physics D: Applied Physics, 29 (12), 1233--1244 (1999).

[4] Wu C. S., Zhong L. M., and Gao J. Q. Visualization of hump formation in high-speed gas metal arc welding. Measurement Science & Technology, 20 (11), 115702 (2009).

[5] Yang D., Wang G., and Zhang G. Thermal analysis for single-pass multi-layer GMAW based additive manufacturing using infrared thermography. Journal of Materials Processing Technology, 244 (1), 215--224 (2017).

[6] Tipi A. R. D., Sani S. K. H., and Pariz N. Frequency control of the drop detachment in the automatic GMAW process. Journal of Materials Processing Technology, 216 (1), 248--259 (2015).

[7] Zhao Y., and Chung H. Numerical simulation of droplet transfer behavior in variable polarity as metal arc welding. International Journal of Heat and Mass Transfer, 111(8), 1129--1141 (2017).

[8] Chen M., Wu C., and Lian R. Numerical analysis of dynamic process of metal transfer in GMAW. Acta Metallrugica Sinica, 40 (11), 1227--1232 (2004).

[9] Tashiro S., and Tanaka M. Modeling of fume formation process in arc welding. Transaction of JWRI, 40 (10), 21--27 (2011).

[10] Dennis J. H., Hewitt P. J., and Redding C. A. A model for prediction of fume formation rate in gas metal arc welding (GMAW), globular and spray models, DC electrode positive. The Annals of Occupational Hygiene, 45 (2), 105--113 (2001).

[11] Haidar J. An analysis of the formation of metal droplets in arc welding. Journal of Physics D Applied Physics, 31 (10), 1233--1244 (1999).

[12] Lei Z. L., Ni L. C., and Li B. W. Numerical simulation of droplet shapes in laser-MIG hybrid welding. Optics & Laser Technology, 88 (1), 1--10 (2017).

[13] Borcia R., Merkt D., and Bestehorn M. A phase-field description of surface-tension-driven instability. International Journal of Bifurcation & Chaos, 14 (12), 4105--4116 (2004).

[14] Guo Z., and Lin P. A thermodynamically consistent phase-field model for two-phase flows with thermocapillary effects. Journal of Fluid Mechanics, 766 (1), 226--271 (2015).

[15] Guo Z., Lin P, and Lowengrub J. S. A numerical method for the quasi-incompressible Cahn–Hilliard-Navier–Stokes equations for variable density flows with a discrete energy law. Journal of Computational Physics, 276 (1), 486--507 (2014).

[16] Hu J., and Tsai H. Heat and mass transfer in gas metal arc welding. Part I the arc. International Journal of Heat and Mass Transfer, 50 (1): 833--846 (2007).

[17] Yue P., Zhou C., and Feng J. J. Sharp-interface limit of the Cahn-Hilliard model for moving contact lines. Journal of Fluid Mechanics, 645 (1), 279--294 (2010).

[18] Jiang Y., Lin P., Guo Z., and Dong S. Numerical simulation for moving contact line with continuous finite element schemes. Communication in Computational Physics, 18 (1), 180--202 (2015).

[19] Yu H., and Yang X. Numerical approximations for a phase-field moving contact line model with variable densities and viscosities. Journal of Computational Physics, 334 (1), 665--686 (2017).

[20] Guo Z., Lin P., and Wang Y. Continuous finite element schemes for a phase field model in two-layer fluid Benard Marangoni convection computations. Computer Physics Communications, 185 (1), 63--78 (2014).

[21] Abels H., Garcke H., and Grun G. Thermodynamically consistent, frame invariant, diffuse interface models for incompressible two phase flows with different densities. Mathematical Models & Methods in Applied Sciences, 22 (3), 1150013 (2012).

[22] Kapahi A., Sambasivan S., and Udaykumar H. S. A three-dimensional sharp interface Cartesian grid method for solving high speed multi-material impact, penetration and fragmentation problems. Journal of Computational Physics, 241 (10), 308--332 (2013).

[23] Hecht F., Pironneau O., Le Hyaric A., Ohtsuka K. FreeFem++ (Version 2.17-1), 2007 (http://www.freefem.org/ff++/ftp/freefem++doc.pdf).

[24] Granger R.A., Fluid mechanics, CBS College, New York, 1985 (Chapter 10).

[25] Zhao Y. and Chung H., Numerical simulation of the transition of metal transfer from globular to spray mode in gas metal arc welding using phase field method, Journal of Materials Processing Tech., 251 (1), 251-261(2018).